
AN INTERPRETABLE NEURAL CONTROL NETWORK WITH ADAPTABLE ONLINE LEARNING FOR SAMPLE EFFICIENT ROBOT LOCOMOTION LEARNING

A PREPRINT

Arthicha Srisuchinnawong

Vidyasirimedhi Institute of Science and Technology
Rayong, Thailand, and
The Mærsk Mc-Kinney Møller Institute
University of Southern Denmark
Odense, Denmark.
arthichas_pro@vistec.ac.th

Poramate Manoonpong

Vidyasirimedhi Institute of Science and Technology
Rayong, Thailand, and
The Mærsk Mc-Kinney Møller Institute
University of Southern Denmark
Odense, Denmark.
poma@mmmi.sdu.dk

January 22, 2025

ABSTRACT

Robot locomotion learning using reinforcement learning suffers from training sample inefficiency and exhibits the non-understandable/black-box nature. Thus, this work presents a novel SME-AGOL to address such problems. Firstly, Sequential Motion Executor (SME) is a three-layer interpretable neural network, where the first produces the sequentially propagating hidden states, the second constructs the corresponding triangular bases with minor non-neighbor interference, and the third maps the bases to the motor commands. Secondly, the Adaptable Gradient-weighting Online Learning (AGOL) algorithm prioritizes the update of the parameters with high relevance score, allowing the learning to focus more on the highly relevant ones. Thus, these two components lead to an analyzable framework, where each sequential hidden state/basis represents the learned key poses/robot configuration. Compared to state-of-the-art methods, the SME-AGOL requires 40 % fewer samples and receives 150 % higher final reward/locomotion performance on a simulated hexapod robot, while taking merely 10 minutes of learning time from scratch on a physical hexapod robot. Taken together, this work not only proposes the SME-AGOL for sample efficient and understandable locomotion learning but also emphasizes the potential exploitation of interpretability for improving sample efficiency and learning performance.

Keywords Locomotion learning · Reinforcement learning · Explainable artificial intelligence · Neural network · Neural control

1 Introduction

Neural networks have demonstrated huge success in a wide range of applications [1–4], including robot locomotion learning [5–15, 15–19]. Locomotion Learning typically employs a reinforcement learning technique [20] to optimize the locomotion control parameters based on the reward function and robot-environment interaction. This learning process, therefore, involves a huge quantity of trial-and-error samples, ranging from 150,000 to 400 million timesteps (1 hr–46 days), even on a simple flat terrain [5–12, 15–19, 21]. There are two main causes for this sample inefficiency.

The first cause lies in the neural network control architecture, where thousands of intertwined parameters need to be trained to properly map input observations (i.e., feedback and robot state) to output motor commands for robot gait generation [5–12, 15–19, 21]. Simplifying the architecture can indeed reduce the control parameters and search space. Training a network with two fully connected hidden layers, with nearly 150,000 parameters [5], reportedly takes 5 million timesteps (≈ 5 hrs). Employing a bio-inspired central pattern generator (CPG) as an internal oscillator for

basic periodic pattern generation and a radial basis function (RBF) to shape the patterns could reduce the number of parameters to 360 [14], thus requiring around 160,000 timesteps (≈ 2 hrs) to obtain a stable gait. Sharing the patterns between diagonal legs (i.e., indirect encoding) could further reduce the number of parameters to 120 [14], potentially accelerating the learning process to 10,000 timesteps (≈ 13 mins). The learning process can be further simplified by predefining intralimb coordination and learning only the control parameters for interlimb coordination. This could involve merely 42 parameters [22] and require approximately 66 timesteps to complete (≈ 5 mins). However, robots trained with these simplified strategies could be limited to certain sets of biased actions or gaits (e.g., bilateral symmetric locomotion [14] or identical leg patterns [22]), leading to less action/gait diversity and adaptability.

The second cause involves the learning algorithm (i.e., the update rule). In policy gradient-based learning [20], a parameter update could be computed from a gradient that maximizes the expected return. This expected return is obtained from an integration, across all possible trajectories, of the product of the probability of each trajectory and its corresponding reward. However, in practical, the expected return must be estimated with a sampling method due to the vast continuous trajectory space and non-differentiable nature of the return. Consequently, many samples need to be acquired as a batch/set of rollouts before performing the update to stabilize and guide the learning process [5–12, 15–19, 21]. This can cause sample inefficiency and may be impractical in real-world applications. To address this issue, some learning studies applied certain assumptions, such as parameter independence [23–25] or a unknown input-output mapping function [22, 26], to simplify the learning rule. Recent locomotion learning approaches have also revisited the use of biased information, such as guided pose [11], to facilitate the optimization process.

While the sample efficiency mentioned above remains an unsolved problem, the black-box characteristic of neural networks has been raised as another issue, where a neural network can produce unreliable results [4]. Therefore, it is essential to equip both the neural network architecture and learning algorithm with interpretability, allowing developers and users to understand and analyze them effectively [4, 27, 28]. As a result, designing decomposable modular neural architectures has been suggested as a solution to obtain an interpretable neural architecture [27], where the network could be divided into modules [2, 3, 29, 30] or two-neuron design operators [31] with specific functionalities. Furthermore, post-hoc explanation techniques, such as local interpretable model-agnostic explanation (LIME) [4], layer-wise relevance propagation (LRP) [32], and guided backpropagation (GBP) [33], have been proposed for unveiling learning algorithms and their results through network attention and key feature interpretation.

Although the locomotion learning performance and interpretability seem to be two different unrelated aspects, we hypothesize that interpretability could also be utilized to facilitate and speed up locomotion learning. Thus, this study proposes efficient neural control and learning mechanisms combining these two aspects. Starting from an interpretable Sequential Motion Executor (SME) architecture (i.e., an interpretable neural control network), each neuron is designed to serve specific functions (i.e., internal state and key pose¹), providing less interference between non-related activities to ease the collective learning [20], as discussed in Section 2.1. An Adaptable Gradient-weighting Online Learning algorithm (AGOL) (i.e., an adaptable online learning rule) is also developed. It can be adapted and scaled according to relevance/importance scores [32, 33], allowing the learning to focus more on highly relevant control parameters, as discussed in Section 2.2.

In summary, the contributions of this work include:

1. An interpretable Sequential Motion Executor (SME) network, along with its design principle, serving as a foundational structure to achieve sample efficiency and enhance locomotion learning.
2. An Adaptable Gradient-weighting Online Learning (AGOL) algorithm, acting as an online control parameter optimizer to achieve sample efficiency and enhance locomotion learning.

In addition to the key contributions, this study also demonstrates the performance of the proposed SME-AGOL mechanisms in hexapod robot locomotion learning in the real world. This demonstration highlights the potential of leveraging interpretability to improve both the sample efficiency and performance of robot locomotion learning.

2 Interpretable Sequential Motion Executor-Adaptable Gradient-weighting Online Learning (SME-AGOL)

In this section, we present the SME-AGOL architecture (Fig. 1a), which consists of the Sequential Motion Executor mechanism (SME, described in Section 2.1) and the Adaptable Gradient-weighting Online Learning mechanism (AGOL, described in Section II-B). The SME acts as neural control for locomotion generation, while the AGOL functions as an online learning algorithm for adapting the control parameters.

¹Here, a key pose refers to a specific robot configuration or a set of joint positions.

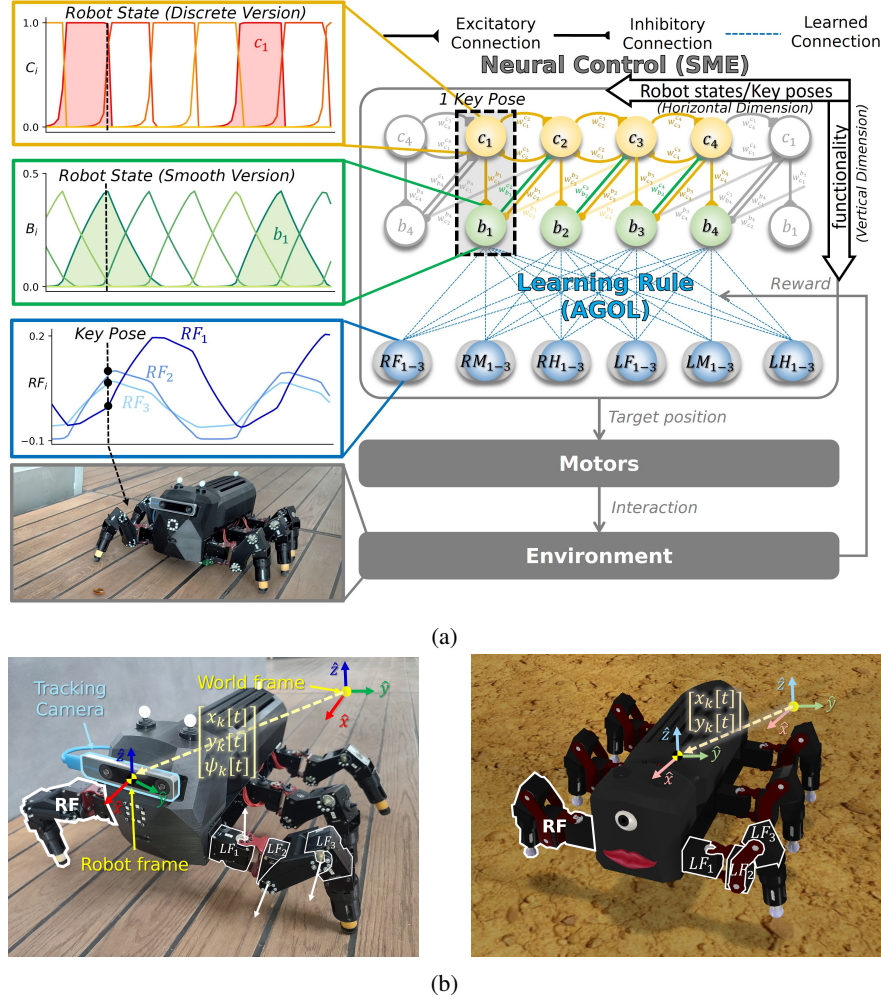


Figure 1: (a) An overview of the Sequential Motion Executor-Adaptable Gradient-weighting Online Learning (SME-AGOL) architecture, presented along with the corresponding signals obtained from three layers, and the experimental hexapod robot platform MORF [34] for the study. The three layers include a central pattern generator layer (c_i , red) providing the discrete (non-smooth) robot states, a basis layer (b_i , green) providing the smooth version of the robot states or the movement bases, and an output layer ($\{M_i\} = \{RF_{1-3}, RM_{1-3}, RH_{1-3}, LF_{1-3}, LM_{1-3}, LH_{1-3}\}$) providing the motor commands (e.g., RF_{1-3} , blue), which can be interpreted as the interpolated key poses. (b) The physical and simulated versions of MORF including the motor positions of a leg, their rotational axes, the RealSense tracking camera, the world frame, the robot frame, and the transformation between the world and robot frames.

To verify the proposed SME-AGOL mechanisms, this study employs a hexapod robot (MORF) [34] with six legs (Fig. 1b), each of which has three active joints: right front leg (RF_{1-3}), right middle leg (RM_{1-3}), right front leg (RH_{1-3}), left front leg (LF_{1-3}), left middle leg (LM_{1-3}), and left front leg (LH_{1-3}). Each joint is controlled by a Dynamixel servo motor, receiving target position commands as input. For sensory feedback, here the robot utilizes two modalities: motor position feedback for low-level PID control and visual odometry feedback for estimating its traveled distance. The traveled distance estimation is used for reward computation of the AGOL. The odometry feedback is obtained from an Intel Realsense tracking camera T265 in the case of a physical robot and computed from the global robot position and orientation in the case of simulation (Coppeliasilim [35] with Mujoco physics engine [36]).

2.1 Sequential Motion Executor (SME) Neural Control

The SME (Fig. 1a) is an interpretable, discrete-time neural control network. It generates target motor position commands based solely on its internal states. The motor commands drive the robot's locomotion. The control network is designed

with two dimensions of interpretability: vertical and horizontal dimensions. The vertical dimension reflects the overall control functionality, while the horizontal dimension encodes the robot’s states or key poses² (robot motion encoding).

Along the vertical dimension, the network consists of three neuron layers: central pattern generator neurons (Cs), basis neurons (Bs), and output neurons (RFs–LHs). Cs provide the central patterns, which are pre-configured to activate sequentially, as depicted in red/yellow (the top left plot in Fig. 1a). These neural activities are subsequently fed to Bs in the basis layer to produce triangle-shaped basis signals, as depicted in green (the middle left plot in Fig. 1a). Accordingly, these Bs are also activated in the same order as Cs; however, they only overlap with their neighbors, providing less interference between non-neighbor bases while maintaining smooth transitions. Finally, the basis activities are mapped to the output motor commands, as depicted in blue (the bottom left plot in Fig. 1a), through the learned connections.

Along the horizontal dimension, each column-wise alignment represents a specific robot state corresponding to a key pose (the black dashed square in Fig. 1a). In this network structure, each column has a central pattern generator neuron that generates a basic, discrete state. This state is then further shaped by the basis neuron into a smoother state. The learned connections (the blue dashed lines in Fig. 1a) encode the joint/motor position commands corresponding to the robot states, where the one from b_i to M_i represents the key pose of joint M_i when b_i fully activates, and M_i denotes the output neurons (i.e., RF_{1-3} , RM_{1-3} , RH_{1-3} , LF_{1-3} , LM_{1-3} , and LH_{1-3}). It should be noted that, in this work, the entire network is updated at 20 Hz, with four sets of neurons ($\{c_i, b_i\}$, $i \in \{1, 2, 3, 4\}$), representing minimal four key poses: two for the swing phase and two for the stance phase, as presented in Fig. 1a.

2.1.1 Central Pattern Generator Neurons (Cs)

Functioning as the internal states of the network, Cs use the corresponding bases to trigger the propagation to the next. The activity of each neuron is governed by:

$$\mathbf{c}[t+1] = \text{sigmoid}(\mathbf{W}_c^c \mathbf{c}[t] + \mathbf{W}_b^c \mathbf{b}[t] + b^c), \quad (1)$$

where $\mathbf{c}[t]$ and $\mathbf{b}_i[t]$ denote the activation vector of the central pattern generator neurons at timestep t ($c_i[t]$) and that of the bases ($b_i[t]$), \mathbf{W}_c^c and \mathbf{W}_b^c denote the connection weight matrices from Cs to Cs and Bs to Cs, respectively (it should be noted that their elements at row i^{th} and column j^{th} are denoted by $w_{c_j}^{c_i}$ and $w_{b_j}^{c_i}$, respectively), and b^c denotes a scalar bias.

The parameters $w_{c_p}^{c_i}$, $w_{c_i}^{c_i}$, $w_{c_n}^{c_i}$, $w_{b_p}^{c_i}$ and b^c , where p , i , and n denote the index of the previous, current, and next neurons in the sequence, are selected analytically such that $c_i[t]$ should:

- be γ when the previous state and previous basis neurons are both active ($c_p[t] = b_p[t] = \iota$) while the others remain inhibited,
- remain inhibited around $-\omega$ when only the previous state is active ($c_p[t] = \iota$),
- remain inhibited around $-\omega$ when only the previous basis is active ($b_p[t] = \iota$),
- be maintained around ω when it is previously active ($c_i[t] = \iota$),
- be inhibited to around $-\omega$ when the next internal state is active ($c_n[t] = \iota$) even if others remain active.

These yield a system of boundary equations as:

$$\begin{bmatrix} \gamma \\ -\omega \\ -\omega \\ \omega \\ -\omega \end{bmatrix} = \begin{bmatrix} \iota & \epsilon & \epsilon & \iota & 1 \\ \iota & \epsilon & \epsilon & \epsilon & 1 \\ \epsilon & \epsilon & \epsilon & \iota & 1 \\ \epsilon & \iota & \epsilon & \epsilon & 1 \\ \iota & \iota & \iota & \iota & 1 \end{bmatrix} \begin{bmatrix} w_{c_p}^{c_i} \\ w_{c_i}^{c_i} \\ w_{c_n}^{c_i} \\ w_{b_p}^{c_i} \\ b^c \end{bmatrix}, \quad (2)$$

where γ refers to the minimum activity of an active neuron, ω refers to a value corresponding to $\text{sigmoid}(\omega) \rightarrow 1$, ι refers to fully excited activity, and ϵ refers to fully inhibited activity.

In this work, the free parameters γ , ω , ι , and ϵ are chosen as 0.5, 8, 0.95, and 0.01, respectively. This yields $w_{c_p}^{c_i}$, $w_{c_i}^{c_i}$, $w_{c_n}^{c_i}$, $w_{b_p}^{c_i}$ and b^c of 8, 25, -32, 8, and -15. With these parameters, the resulting four central pattern generator outputs ($c_{1-4}[t]$) are illustrated in Fig. 1a (radish/yellowish). These output signals are then fed to the basis neurons to produce bases for output mapping.

²Here, a key pose refers to a specific robot configuration or a set of joint positions.

2.1.2 Basis Neurons (Bs)

Receiving the internal states/central pattern generator outputs, the basis neurons are formulated as Eq. 3 to produce triangular periodic signals, interpreted as key poses (sets of all joint positions).

$$\mathbf{b}[t+1] = \text{ReLU}(\mathbf{W}_c^b \mathbf{c}[t] + \mathbf{W}_b^b \mathbf{b}[t]), \quad (3)$$

where $\mathbf{c}[t]$ and $\mathbf{b}_i[t]$ denote the activation vector of the central pattern generator outputs at timestep t ($c_i[t]$) and that of the bases ($b_i[t]$), $\text{ReLU}()$ denotes the rectified linear unit function, and \mathbf{W}_c^b and \mathbf{W}_b^b denote the connection weight matrices from Cs to Bs and Bs to Bs, respectively (their elements are denoted by $w_{c_j}^{b_i}$ and $w_{b_j}^{b_i}$).

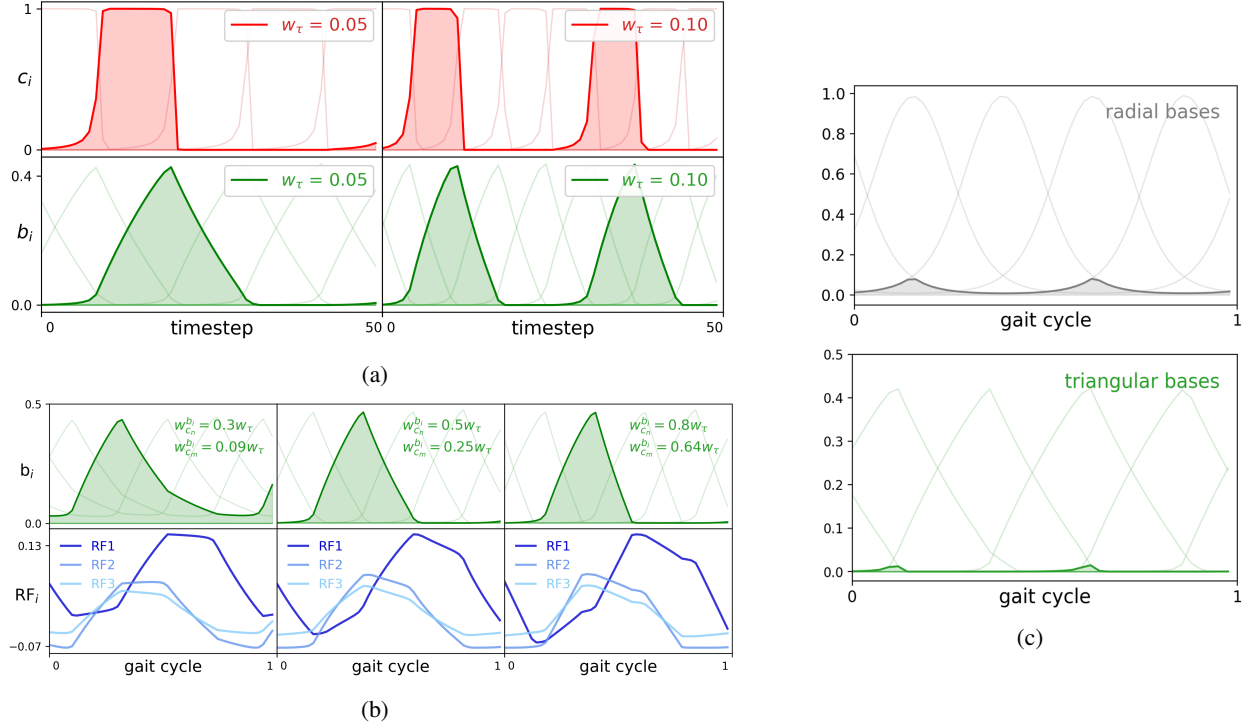


Figure 2: (a) Central pattern generator neurons/internal states (c_i) and bases (b_i) obtained from SME where $w_\tau =$ (left) 0.05 and (right) 0.10. (b) Intersection between two non-neighbor (left) radial bases and (right) equivalent triangular bases. (c) Bases (b_i) and outputs (RF_i) obtained from SME where $w_{c_n}^{b_i}$ and $w_{c_m}^{b_i}$ are set as (left) $0.3w_\tau$ and $0.09w_\tau$, (middle) $0.5w_\tau$ and $0.25w_\tau$, and (right) $0.8w_\tau$ and $0.64w_\tau$.

The parameters $w_{c_i}^{b_i}$ and $w_{b_i}^{b_i}$, are selected as w_τ and $1 - w_\tau$ such that each basis neuron performs lowpass filtering of the corresponding central pattern generator neuron/internal state. Thus, w_τ is another free parameter, controlling the transition speed/walking frequency, as illustrated in Fig. 2a. In this work, w_τ is selected as 0.05 to obtain a gait frequency of 0.3 Hz.

The parameters $w_{c_n}^{b_i}$ and $w_{c_m}^{b_i}$, where n and m denote the index of the next and second neurons in the sequence, are then selected empirically, as illustrated in Fig. 2b, to shape the bases. $w_{c_n}^{b_i}$ and $w_{c_m}^{b_i}$ are set as $0.5w_\tau$ and $0.25w_\tau$, respectively, to reduce interference/intersection between non-neighbors (Fig. 2b-left and Fig. 2c) and discontinuous outputs (Fig. 2b-right). With this setup, the resulting triangular bases have 33% less intersection between non-neighbor bases (7% of the time, p-value < 0.05, Mann-Whitney U test) than those of equivalent radial bases employed in [14] (40% of the time), as shown in Fig. 2c. At each timestep, these bases are then mapped to the outputs through learned connections, where less interference can reduce the number of active bases, thereby decreasing the number of relevant parameters/connections weights that need to be updated. Consequently, this mechanism can identify the important control parameters (here, output mapping weights), facilitating the learning process. In other words, it encourages the learning process to focus more on a few highly relevant control parameters at each time/iteration, as shown in Fig. 2c when compared with CPGRBF [14].

2.1.3 Output Neurons (RFs–LHs)

In this work, a learned weight matrix \mathbf{W}_b^o (18 rows/outputs \times 4 columns/key poses) translates the bases to 18 outputs, employed as motor position commands (i.e., direct encoding [14]). The outputs are computed according to:

$$\mathbf{o}[t+1] = \text{clip}(\mathbf{W}_b^o \mathbf{b}[t], -\alpha_{\max}, \alpha_{\max}), \quad (4)$$

where $\mathbf{o}[t]$ denotes the output vector t ($RF_1[t]$ – $LH_3[t]$), $\mathbf{b}_i[t]$ denotes the activation vector of the bases at timestep t ($b_i[t]$), $\text{clip}()$ denotes the saturation function, ensuring that the outputs are between the joint limit $(-\alpha_{\max}, \alpha_{\max})$. α_{\max} is 0.3 in this work, and \mathbf{W}_b^o denotes the connection weight matrices from Bs to the outputs.

As each b_i neuron is activated one after another, they can be interpreted as the activation of certain key poses. Four basis activities (b_{1-4}) are then mapped to 12 motor positional commands via the learned weights/connections between the basis layer (b_i s) and the output layer (RF–LH). As these 4×12 weight values are learned independently (i.e., direct encoding [14]), the robot can learn/adjust each leg patterns independently. Therefore, inter-leg coordination is achieved by adjusting/learning these 4×12 mapping weight values, as shown in Sections S1 and S2 in the supplementary material. Leg coordination pattern can be obtained through swapped \mathbf{W}_b^o weight values, as shown in Figs. S1–S3 in Section S1 in the supplementary material, while different shape signals can be obtained through different \mathbf{W}_b^o weight values, as shown in Fig. S4 in Section S2 in the supplementary material. In this work, the weight matrix \mathbf{W}_b^o was trained with the AGOL to achieve leg coordination and different leg patterns automatically based in the rewards obtained from trial-and-error, as described in the following section.

2.2 Adaptable Gradient-weighting Online Learning (AGOL)

During the training, a sampling method is applied along with the assumption of a deterministic environment ($\nabla_{\theta} \ln p(s_0) = 0$ and $\nabla_{\theta} \ln p(s_{t+1}|s_t, \tilde{a}_t) = 0$), yielding:

$$\begin{aligned} \Delta\theta &\approx \eta_{\theta} \sum_{\tau} \nabla_{\theta} \ln \left(p(s_0) \prod_i p(s_{t+1}|s_t, \tilde{a}_t) p(\tilde{a}_t|\theta) \right) R_t, \\ &\approx \eta_{\theta} \sum_{\tau} \sum_t \nabla_{\theta} \ln p(\tilde{a}_t|\theta) R_t, \end{aligned} \quad (5)$$

where $\Delta\theta$ denotes the weight update, η_{θ} denotes the learning rate, τ denotes a trajectory, $p(s_0)$ denotes the probability distribution of being at the state s_0 , $p(s_{t+1}|s_t, \tilde{a}_t)$ denotes the probability distribution of being at s_{t+1} given the previous state s_t and explored action \tilde{a}_t , $p(\tilde{a}_t|\theta)$ denotes the probability distribution of performing explored action \tilde{a}_t given network parameter θ , and R_t denotes the corresponding return computed from the summation of all the rewards obtained ($R = \sum_{t'} r_{t'}$).

In action space exploration learning algorithms, like policy gradient (PG) [23], $p(\tilde{a}_t|\theta)$ is estimated with a normal distribution of explored action \tilde{a}_t given actual differentiable action a_t (i.e., $\mathcal{N}(\tilde{a}_t; a_t, \sigma_a)$ or $\pi_{\theta}(\tilde{a}_t|a_t)$), while proximal policy optimization (PPO) [25] further incorporates importance sampling between old and new policies. However, [24, 37, 38] reported that exploring policy in the parameter space outperforms the action space counterparts due to consistency. As a result, a policy gradient with parameter-based exploration (PGPE) [24] revises the learning rule in Eq. 5 by performing exploration in the parameter space while assuming $\nabla_{\theta} \ln p(\tilde{a}_t|\theta) = 0$ due to the deterministic relationship between \tilde{a}_t and $\tilde{\theta}_t$. This yielded:

$$\begin{aligned} \Delta\theta &\approx \eta_{\theta} \sum_{\tau} \sum_t \nabla_{\theta} \ln \left(p(\tilde{a}_t|\tilde{\theta}_t) p(\tilde{\theta}_t|\theta) \right) R_t, \\ &\approx \eta_{\theta} \sum_{\tau} \sum_t \nabla_{\theta} \ln \mathcal{N}(\tilde{\theta}_t; \theta, \sigma_{\theta}) R_t, \\ &\approx \eta_{\theta} \sum_{\tau} \sum_t \frac{(\tilde{\theta}_t - \theta)}{\sigma_{\theta}^2} R_t, \end{aligned} \quad (6)$$

where $\Delta\theta$ denotes the weight update, η_{θ} denotes the learning rate, τ denotes a trajectory, $p(\tilde{a}_t|\tilde{\theta}_t)$ denotes the probability distribution of explored action \tilde{a}_t given explored parameter $\tilde{\theta}_t$, $p(\tilde{\theta}_t|\theta)$ denotes the probability distribution of explored parameter $\tilde{\theta}_t$ given parameter θ and standard deviation σ_{θ} ($\mathcal{N}(\tilde{\theta}_t; \theta, \sigma_{\theta})$), and R_t denotes the return.

From Eq. 6, in the policy gradient with parameter-based exploration (PGPE) [24], R_t is replaced with the difference between the obtained reward and estimated baseline (advantage, A_t), whereas, in the policy improvement with

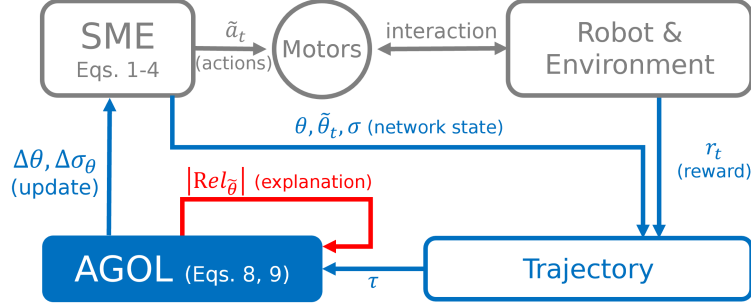


Figure 3: Online locomotion learning process. Firstly, the robot interacts with the environment through the use of explored action \tilde{a}_t generated from the SME neural control. Secondly, the AGOL learning rule updates the SME control parameters using the samples from the trajectory τ , consisting of the reward obtained from the interaction with environment r_t , the network state (including the parameters θ , explored parameters $\tilde{\theta}_t$, and exploration standard deviation σ_θ), and the relevance explanation $|\text{Rel}_{\tilde{\theta}}|$ computed from the network state.

black-box optimization (PIBB) [26], it is substituted with the ranking score. While these approaches assume that $\nabla_\theta \ln p(\tilde{a}_t|\tilde{\theta}_t) = 0$, the parameter θ is updated even if it does not contribute to the explored action \tilde{a}_t .

Therefore, as an improvement, the learning rule in Eq. 6 can be modified by introducing the (absolute) relevance of the parameter ($|\text{Rel}_{\tilde{\theta}}|$), according to:

$$\Delta\theta \approx \eta_\theta \sum_\tau \sum_t |\text{Rel}_{\tilde{\theta}}| \frac{(\tilde{\theta}_t - \theta)}{\sigma_\theta^2} A_t, \quad (7)$$

where $\Delta\theta$ denotes the weight update, η_θ denotes the learning rate, τ denotes a trajectory, \tilde{a}_t denotes the explored action according to the explored parameter $\tilde{\theta}_t$, σ_θ denotes the exploration standard deviation, θ denotes the actual network parameter, and A_t denotes the corresponding advantage estimated from the reward/return R_t and the baseline (e.g., average reward).

To exploit PyTorch autograd [39] for efficient computation, this work substitutes $\text{Rel}_{\tilde{\theta}}$ with the gradient of the action with respect to the parameters ($|\nabla_{\tilde{\theta}} \tilde{a}_t|$), according to:

$$\Delta\theta \approx \eta_\theta \sum_\tau \sum_t |\nabla_{\tilde{\theta}} \tilde{a}_t| \frac{(\tilde{\theta}_t - \theta)}{\sigma_\theta^2} A_t, \quad (8)$$

where $\Delta\theta$ denotes the weight update, η_θ denotes the learning rate, τ denotes a trajectory, \tilde{a}_t denotes the explored action according to the explored parameter $\tilde{\theta}_t$, σ_θ denotes the exploration standard deviation, θ denotes the actual network parameter, and A_t denotes the corresponding advantage estimated from the reward/return R_t and the baseline (e.g., average reward).

Using this learning rule, at each t , the output gradient cannot be backpropagated to the parameters that do not contribute to the outputs/actions, resulting in $|\nabla_{\tilde{\theta}} \tilde{a}_t| \rightarrow 0$. Moreover, the added gradient upweights the updates of more relevant parameters and downweights those of less relevant parameters. Intuitively, this learning rule equips robots with the ability to explain the relevance of each parameter to itself and scale the update accordingly, as illustrated in Fig. 3, allowing the robot to focus on a few important parameters each time.

Following a similar procedure, the exploration weights can also be adapted online ($\Delta\sigma_\theta$) using the gradient with respect to the exploration standard deviation ($\nabla_{\sigma_\theta} \ln p(\tau|\theta)$) and an exploration adaptation/learning rate (η_σ), yielding:

$$\Delta\sigma_\theta \approx \eta_\sigma \sum_\tau \sum_t \left(|\nabla_{\tilde{\theta}} \tilde{a}_t| \frac{(\tilde{\theta}_t - \theta)^2 - \sigma_\theta^2}{\sigma_\theta^3} A_t \right). \quad (9)$$

In this work, to learn hexapod locomotion, this learning rule is applied to update the connection weights (\mathbf{W}_b^o), mapping the bases to outputs, all initialized as zero. Two variants of AGOL are also studied. The first (AGOL) performs online learning by updating the parameter after each episode ends, while the second (Added Gradient Learning or AGL) performs batch learning by updating the parameter after certain episodes (here, eight episodes are sufficient for batch learning as shown in [14]).

3 Experiments and Results

To verify the proposed SME-AGOL, two experiments were conducted. The first experiment (Section 3.1) compared five different state-of-the-art learning algorithms, cross-implemented with two implementations (batch and online learning) and two neural control architectures, on a simulated hexapod robot, where reward and sample efficiency (learning speed) were selected as the comparison metrics. The second experiment (Section 3.2) then extended this to a physical robot to validate the SME-AGOL performance in the real world.

3.1 Simulation Experiment

In this experiment, two neural control architectures (SME and the state-of-the-art control (CPGRBF) [14] in Section S3 of the supplementary document) were compared due to their comparable mapping process (i.e., radial bases in CPGRBF versus triangular bases in SME) and having the identical parameter numbers (i.e., 72 parameters). For the learning, two action space exploration learning algorithms (policy gradient (PG) [23] and proximal policy optimization (PPO) [25]) along with three parameter space exploration learning algorithms (policy improvement with black-box optimization (PIBB) [26], policy gradient with parameter-based exploration (PGPE) [24], and the proposed AGOL), were cross-implemented with the control architectures. For each learning algorithm, batch learning (Algorithm 1) and online learning (Algorithm 2) were also included. For clarity, ⁺ denotes the online learning implementations.

Algorithm 1 Batch learning implementation

```

initialize all parameters to zero.
while episode  $\leq$  100 do
  reset the environment.
  while  $t \leq 70$  do
    update the network, execute  $\tilde{a}_t$ , and get  $r_t$ .
    append the network state,  $\tilde{a}_t$ , and  $r_t$  to  $\tau$ .
  end while
  if every 8 episodes, i.e.,  $(\text{episode} \% 8) = 7$  then
    update the parameters (e.g., with Eq. 8).
    empty  $\tau$ .
  end if
end while

```

Algorithm 2 Online learning implementation

```

initialize all parameters to zero.
while episode  $\leq$  100 do
  reset the environment.
  while  $t \leq 70$  do
    update the network, execute  $\tilde{a}_t$ , and get  $r_t$ .
    append the network state,  $\tilde{a}_t$ , and  $r_t$  to  $\tau$ .
  end while
  if  $\tau$  size  $>$   $70 \cdot 8$  then remove  $\tau_0 - \tau_{70}$ .
  update the parameters (e.g., with Eq. 8).
end while

```

In total, this simulation experiment consisted of 20 testing conditions. The hyperparameters of each testing condition were obtained from a grid search, and the testing was repeated 10 times. Each repetition took 100 episodes with 70 timesteps per episode, and the update uses the data from 8 previous episodes/runs. To reduce the randomness for the comparison, the robot state and the neural control state were reset every episode. The reward and advantage estimate were computed from:

$$A_t = (R_t - \mu_{R_t}) / \sigma_{R_t}, \quad (10)$$

$$R_t = \sum_{t'=t}^{70} r_{t'}, \quad (11)$$

$$r_t = (x[t] - x[t-1]) - (y[t] - y[t-1]), \quad (12)$$

where A_t , R_t , and r_t denote the advantage, return, and reward at timestep t in trajectory τ , respectively, μ_{R_t} and σ_{R_t} denote the average and standard deviation computed from all the returns at timestep t , and $x[t]$ and $y[t]$ denote the robot position along the x-axis (forward/backward direction) and y-axis (sideways direction) at timestep t in trajectory τ , as shown in Fig. 1b.

Table 1: Final rewards and the number of episodes before receiving an episodic reward above 0.2 (i.e., the reward value achievable within the first 100 episodes by half of the methods tested in this work). It should be noted that the highest final reward and the lowest number of episodes before receiving an episodic reward above 0.2 are highlighted in bold. The significant levels of all comparison pairs are depicted in Fig. 4.

Learning algorithm	Final reward		# episodes to reach 0.2	
	CPGRBF	SME	CPGRBF	SME
PG	-0.01	-0.02	n/a	n/a
PG⁺	-0.02	0.08	n/a	n/a
PPO	0.01	0.06	n/a	n/a
PPO⁺	-0.04	0.0	n/a	n/a
PIBB	0.23	0.2	60	79
PIBB⁺	0.34	0.29	49	60
PGPE	0.31	0.33	71	64
PGPE⁺	0.32	0.42	54	40
AGL	0.36	0.43	66	52
AGOL	0.35	0.58	54	35

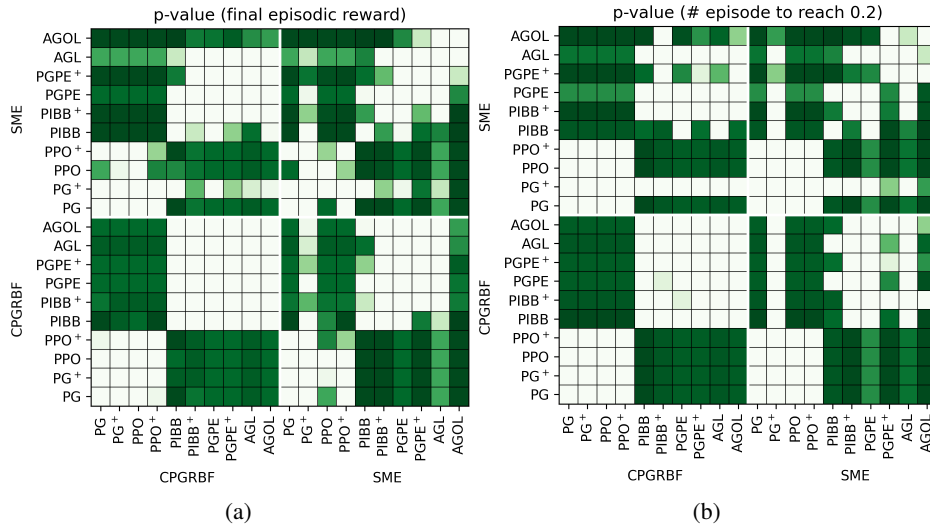


Figure 4: Mann-Whitney U test p-value corresponding to all comparison pairs in terms of (a) the final episodic reward and (b) the number of episodes taken to reach the reward of 0.2, where each cell intensity represents the significant level. The white cells indicate the pairs with p-value ≥ 0.05 (insignificant comparison), the light green cells indicate the pairs with low p-value, i.e., p-value < 0.05 (significant comparison), and the dark green cells indicate the pairs with very low p-value, i.e., p-value $\ll 0.05$ (highly significant comparison).

In this experiment, the comparison was performed using two matrices. The first is the final episodic reward, indicating the performance. The second is the number of episodes taken to obtain the same episodic reward value, indicating the learning speed. In this experiment, an episodic reward threshold of 0.2 was selected (i.e., a robot forward speed of 0.2 m/episode or ≈ 20 cm/gait cycle) This threshold is equivalent to 40% of the theoretical maximum of the robot walking speed (V_{\max}), which is computed from $V_{\max} = 2L_{\max}$, where L_{\max} is the maximum leg length of the robot (here, 25 cm), and a forward speed of $\approx 60\%$ of its body length per gait cycle (here, 30 cm). The results of this experiment are summarized in Table 1 and presented in details in Fig. 5a–Fig. 6b. Besides, a video of this simulation experiment can be seen at https://youtu.be/Svz5H2_MDew.

Considering first the CPGRBF neural control architecture, the combination of CPGRBF-AGL received the highest average final reward of around 0.36, reaching 0.2 after 66 episodes. The second-best performance was obtained from the one with CPGRBF-AGOL (online learning), which received a slightly lower average final reward of 0.35, reaching

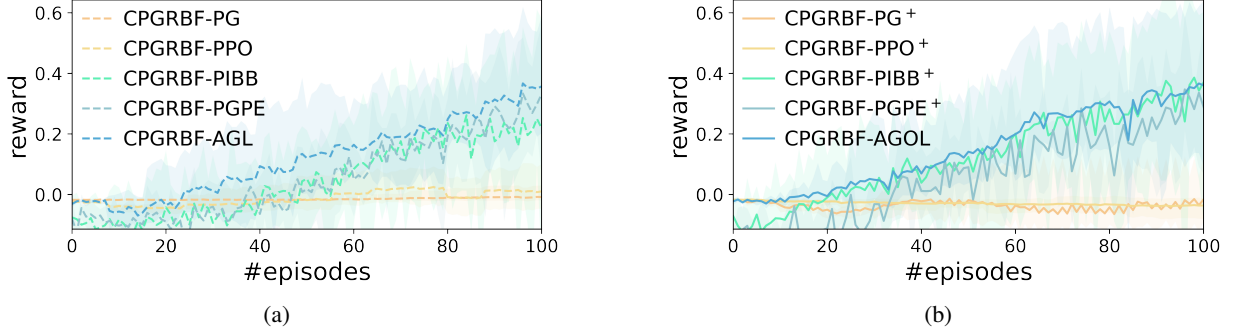


Figure 5: Average episodic rewards, i.e., learning curves and the corresponding min-max range (shade) obtained from five different learning algorithms validated with the CPGRBF neural control architecture [14] under two implementations: (a) batch learning and (b) online learning.

a reward of 0.2 after 54 episodes. Two groups of performances can be observed in both Fig. 5a and Fig. 5b (p -value < 0.05 , Kruskal-Wallis test). In the first group, using CPGRBF along with parameter space learning algorithms (PIBB, PIBB⁺, PGPE, PGPE⁺, AGL, and AGOL) yielded average final rewards above 0.2 with no significant difference within the group (p -value > 0.05 , Kruskal-Wallis test). In the second group, using CPGRBF along with all action space learning algorithms (PG, PG⁺, PPO, and PPO⁺) failed to produce a reward higher than 0.2 with no significant difference within the group (p -value > 0.05 , Kruskal-Wallis test).

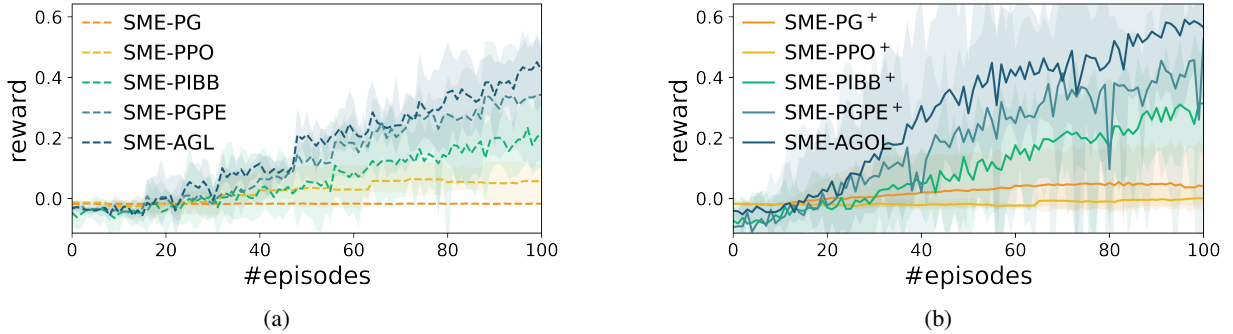


Figure 6: Average episodic rewards, i.e., learning curves and the corresponding min-max range (shade) obtained from five different learning algorithms validated with the proposed SME neural control architecture under two implementations: (a) batch learning and (b) online learning.

Moving to the SME, the combination of SME-AGOL (the proposed method) received the highest average final reward of around 0.58 (60% greater than the one from SME-AGL, p -value < 0.05 , Mann-Whitney U test), where the reward reached 0.2 after 35 episodes. The second-best performance is from the one with SME-AGL, which received an average final reward of 0.43, reaching a reward of 0.2 after 52 episodes. While SME-AGOL and SME-AGL remarkably outperformed the other combinations (p -value < 0.05 , Mann-Whitney U test), there were no significant differences between the performances of SME-AGOL and SME-AGL (p -value > 0.05 , Mann-Wallis test). Two groups of performances can be observed in Fig. 6a and Fig. 6b in a similar way to the previous results; however, the observable difference between the batch parameter space exploration learning and online parameter space exploration learning was presented (p -value < 0.05 , Kruskal-Wallis test). Batch learning (SME-PIBB, SME-PGPE, and SME-AGL) received the reward values between 0.2 and 0.43, while online learning (SME-PIBB⁺, SME-PGPE⁺, and SME-AGOL) received between 0.29–0.58, or rather 15% more.

Comparing the neural control architectures, i.e., between Fig. 5 and Fig. 6, the proposed SME neural control generally outperforms the state-of-the-art CPGRBF neural control by 30% in parameter space learning, where the average final rewards are all beyond 0.2 (p -value < 0.05 , Kruskal-Wallis test). SME might not be suitable for implementation with PIBB, PIBB⁺, PGPE, and PGPE⁺ since they yield a insignificantly different results compared to those with CPGRBFN (p -value > 0.05 , Mann-Whitney U test). However, it achieves significant improvements of 65% with AGOL (p -value < 0.05 , Mann-Whitney U test). It should also be noted that SME-AGOL achieves an average final reward of more than

150 % and uses 40 % less time/sample to achieve a reward of 0.2 than the CPGRBF-PIBB, employed in [14] (p-value < 0.05, Mann-Whitney U test).

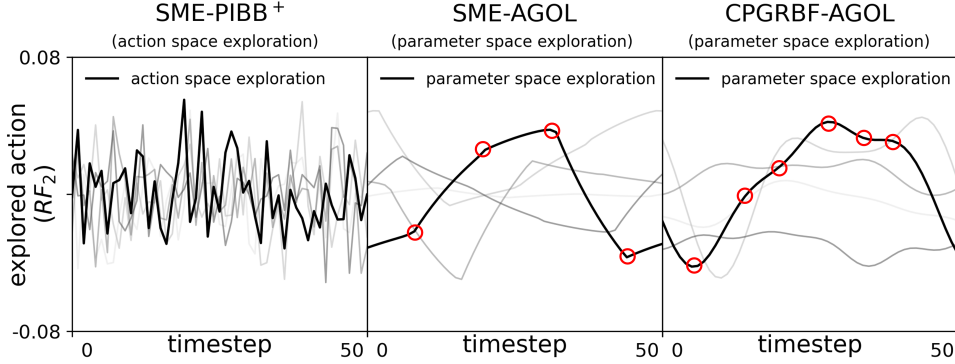


Figure 7: Five examples of the explored robot joint trajectories during the first learning episodes obtained from (left) an action space exploration learning algorithm (SME-PIBB⁺), (middle) a parameter space exploration learning algorithm implemented with SME (SME-AGOL), and (right) a parameter space exploration learning algorithm implemented with CPGRBF neural control (CPGRBF-AGOL). It should be noted that the estimated key poses (i.e., where the trajectory slope changes significantly) are highlighted by the red circles.

To analyze the results, Fig. 7 plots different explored trajectories obtained from action space exploration and parameter space exploration. The former approach attempts different noisy joint trajectories, which causes the learning algorithms like PG and PPO to struggle in computing the updated direction, especially when using fewer samples from eight previous episodes, receiving a lower reward as a consequence. In contrast, the latter approach attempts relatively more consistent explorations: SME-AGOL learns to modify four key points, whereas CPGRBF-AGOL learns to bend the curve, equivalent to modifying 4–7 key points (p-value < 0.05, Mann-Whitney U test), as shown in Fig. 7. Accordingly, parameter space exploration outperforms action space exploration, while SME outperforms the CPGRBF under most conditions.

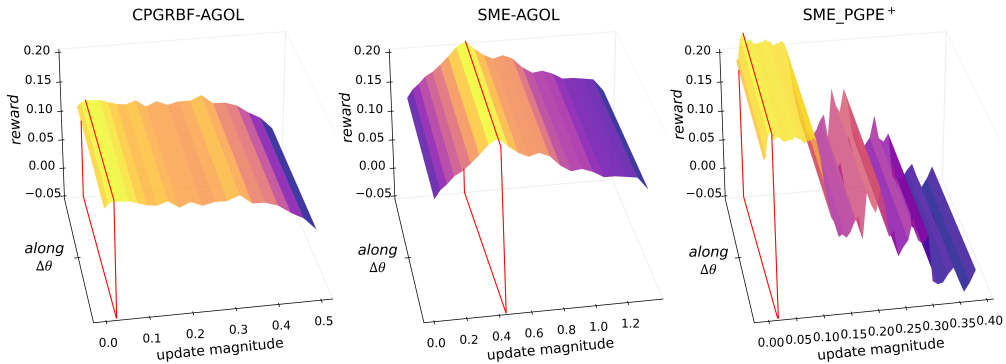


Figure 8: Reward landscape [40] estimated along the update direction $\Delta\theta$ of (left) CPGRBF-AGOL, (middle) SME-AGOL, and (right) SME-PGPE⁺, where the parameter $\theta = \mathbf{W}_b^o$.

To further analyze the accuracy of gradient estimation, Fig. 8 plots three reward landscapes, estimated along the three update directions obtained from CPGRBF-AGOL, SME-AGOL, and SME-PGPE⁺ after 50 episodes. This visualization reveals that CPGRBF-AGOL (left) and SME-PGPE⁺ (right) have an optimal update magnitude of around 0.03; besides, the landscapes have multiple bumps/local maximums. This is due to high interference between radial bases in the former approach (Fig. 2c) and interference from less relevant parameters in the latter approach (Section 2.2). In comparison, SME-AGOL (middle), which has the correction for non-neighbor basis interference and less relevant parameters, yields a more accurate reward update estimation with comparatively fewer bumps/local maximums and an optimal step of slightly above 0.4 (≈ 10 times higher, p-value < 0.05, Mann-Whitney U test).

3.2 Physical Robot Experiment

Extending from the simulation experiment, the aim of the physical experiment was to demonstrate locomotion learning with SME-AGOL and adaptive exploration (Eq. 9) on a physical hexapod robot. The locomotion learning with the physical robot and SME-AGOL was repeated 10 times, following Algorithm 3 with the empirically chosen learning rate of $\eta_\theta = 0.5$ and $\eta_\sigma = 0.1$. Due to the space limit of the experimental area, the experiment was paused when the robot reached the end of the testing platform and continued when moving it manually to the starting location. Each repetition took 200 episodes with 70 timesteps per episode, the data from 8 previous episodes, and without robot state/network state reset.

Algorithm 3 SME-AGOL implementation (physical robot)

```

initialize all parameters to zero.
while true do
  while  $t \leq 70$  ( $\approx 1$  gait cycle) do
    update the network (Eqs. 1–4) and execute  $\tilde{a}_t$ .
    compute  $r_t$  according to Eq. 13.
    append the network state,  $\tilde{a}_t$ , and  $r_t$  to  $\tau$ .
  end while
  if  $\tau$  size  $> 70 \cdot 8$  then remove  $\tau_0 - \tau_{70}$ .
  compute advantage according to Eqs. 14.
  update the parameters with Eqs. 8 and 9.
  update the baseline estimation by minimizing Eq. 16.
end while

```

All parameters were initialized as zero before three iterative steps were performed. This process was updated until the end of the experiment. First, the robot performed exploration for 70 timesteps (≈ 1 gait cycle), by executing explored actions (\tilde{a}_t) obtained from the SME network. The reward (r_t) was then computed according to:

$$r_t = \Delta x[t] \cos(\Delta\psi[t]) + \Delta y[t] \sin(\Delta\psi[t]), \quad (13)$$

where r_t denote the reward at timestep t , while $\Delta x[t]$, $\Delta y[t]$, and $\Delta\psi[t]$, respectively denote the robot displacement at timestep t in x direction, y direction, and yaw orientation. In this work, $\Delta x[t] = x[t] - x[t-1]$, $\Delta y[t] = y[t] - y[t-1]$, and $\Delta\psi[t] = \psi[t] - \psi[t-1]$, where the estimated robot pose ($x[t]$, $y[t]$, and $\psi[t]$) are obtained from the tracking camera, as shown in Fig. 1b. Subsequently, the network states (i.e., activities and parameters), explored actions, and rewards were appended to the trajectories/training samples.

Second, using the training samples from the previous 8 episodes, the advantage values were estimated according to:

$$A_t = (R_t - \mathbf{W}_b^v \mathbf{b}[t]) / \text{RMS}_\tau(R_t - \mathbf{W}_b^v \mathbf{b}[t]), \quad (14)$$

$$R_t = \sum_{t'=t}^{70} r_{t'}, \quad (15)$$

where A_t , R_t , and r_t denote the advantage, return, and reward at timestep t in the trajectory τ , respectively, $\mathbf{W}_b^v \mathbf{b}[t]$ denotes the baseline, $\text{RMS}_\tau(\cdot)$ denotes the root-mean-square function computed over the trajectory τ , $\mathbf{b}[t]$ denotes the activity vector of the bases ($b_i[t]$) at timestep t in trajectory τ , and \mathbf{W}_b^v the mapping weights from Bs to baseline prediction. Given that this advantage estimation incorporates the predicted baseline/expected value at each specific state, the robot learning can operate without the robot state reset, which is practical for physical robot learning.

Third, the policy parameters (i.e., action generation-related parameters) were updated according to the learning rule in Eq. 8 and the exploration parameters were updated according to the learning rule in Eq. 9. This was then followed by updating the baseline prediction, which was performed using gradient descent with a learning rate of 0.05 to minimize the mean square error loss:

$$\mathcal{L} = \text{MSE}_\tau(R_t - \mathbf{W}_b^v \mathbf{b}[t]), \quad (16)$$

where \mathcal{L} denotes the loss function and $\text{MSE}_\tau(\cdot)$ denotes the mean square error between the actual return R_t and the baseline prediction $\mathbf{W}_b^v \mathbf{b}[t]$, averaged over a trajectory τ .

The locomotion learning result is presented in Fig. 9, and a supplementary video can be viewed at https://youtu.be/Svz5H2_MDew, while the corresponding speed (i.e., computed from the reward) is provided in Fig. 10.

Fig. 10 presents that the average speed starts around 0.0 cm/s, indicating that locomotion learning begins without any pre-trained knowledge. The robot then takes merely 20 episodes of trial-and-error (≈ 35 s) before it starts moving

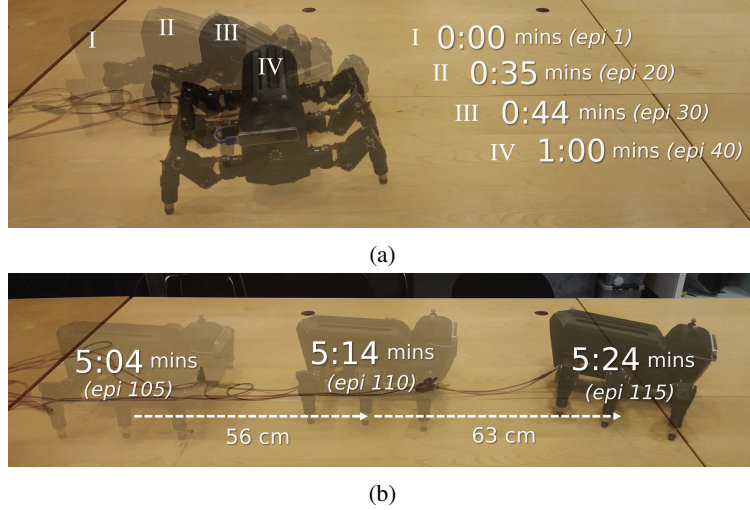


Figure 9: Snapshots from a trial of physical robot locomotion learning (a) during the first 40 episodes and (b) between 105 episodes and 115 episodes. The video of the experiment is available at https://youtu.be/Svz5H2_MDew.

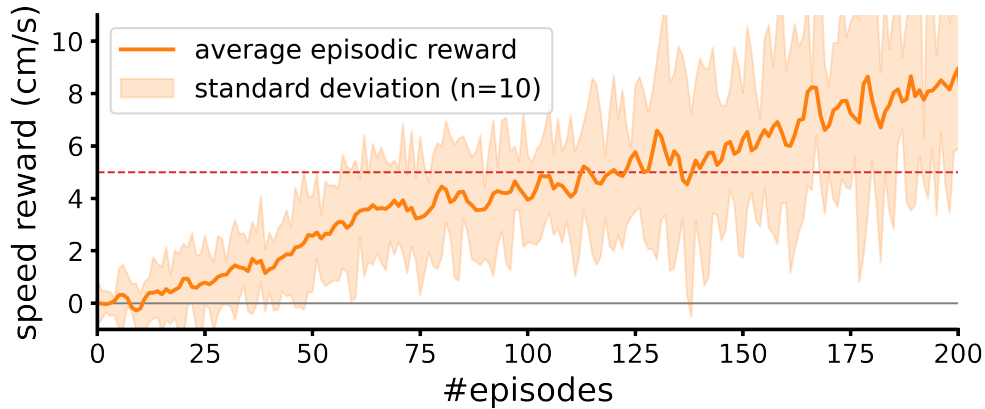


Figure 10: Average episodic reward obtained from 10 repetitions of physical robot locomotion learning, along with the standard deviation. The red dashed line indicates a locomotion speed of 5 cm/s, which is also demonstrated by the same physical robot with a manually designed locomotion controller presented in [30].

forward, receiving a speed of nearly 1.0 cm/s, as also shown in Fig. 9a. During the first 40 episodes (≈ 1 min), the robot exhibited a small positive speed of almost 2.0 cm/s while turning to the right, as shown in Fig. 9a, due to the poor coordination between left and right legs. After 50 subsequent episodes (≈ 2 mins), the robot’s curved locomotion path was corrected, and it eventually developed almost straight locomotion with a speed of around 5 cm/s. Additionally, Fig. 9b illustrates that the robot walked for 56 cm in 10 s between the 105th episode and 110th episode, equivalent to the one measured from the same physical robot with a manually designed locomotion controller demonstrated in [30] (i.e., ≈ 5 cm/s). The robot then maintained straight locomotion and continued improving its speed, resulting in an improved travel speed of 63 cm in 10 s around 115 episodes, as illustrated in Fig. 9b. By 200 episodes, the robot achieved an average speed of slightly above 8 cm/s (between 6 cm/s to 11 cm/s in 10 experiment trials).

In order to analyze the physical robot locomotion learning, Fig. 11 plots the evolution of leg kinematics and adaptive exploration rates obtained from a locomotion learning trial. The leg kinematics is visualized using the output mapping connection weights \mathbf{W}_b^o (18 motor positions/rows \times four key poses/columns) along with the kinematics model, while the adaptive exploration rates of the swing joints (e.g., RF_1) and leg lifting joints (e.g., RF_2 and RF_3) plotted directly from the moving averages of σ_{LF_1} and σ_{RF_1} and those σ_{LF_2/LF_3} and σ_{RF_2/RF_3} , respectively.

Fig. 11 reveals that the robot autonomously varies its exploration rate, and this could be used to interpret the focus of the learning. For instance, the overlapping exploration rates between swing joints (e.g., RF_1 , black lines) and leg lifting

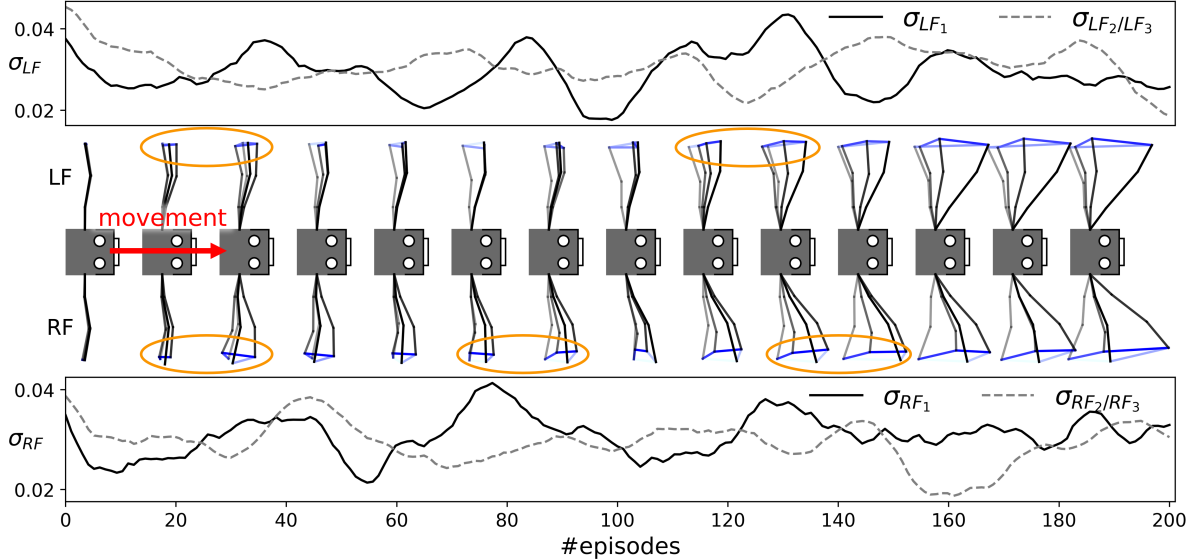


Figure 11: Graphical representation of the top view robot kinematics and evolution of the adaptive exploration rates of the left front (LF) and right front (RF) legs obtained from the locomotion learning in Fig. 9. In the graphical representation, four key poses are represented by four gray shades: black \rightarrow dark gray \rightarrow gray \rightarrow light gray \rightarrow back to black, with the corresponding foot heights represented by blue shades: dark blue indicating a relatively lower foot path (stance phase), and light blue a relatively higher foot path (swing phase). For visualization purposes, small offsets (i.e., 0.1 rads) are added to all joints.

joints (e.g., RF_2 and RF_3 , gray dashed lines) indicate that the robot repeatedly shifts its focus between learning the lifting actions and swinging actions. In the first 30 episodes, greater exploration of leg lifting joints (gray dashed lines above black lines) suggests a focus on adjusting the lifting pattern. After obtaining a proper lifting pattern (e.g., after 30 episodes, as also shown in Fig. 9), focus shifted toward the swing/shoulder joints (black lines above gray dash) to increase the swing amplitude. This process is repeated for around 30, 80, and 130 episodes, while an increase in swing amplitudes can be observed from the leg kinematics for most of the time due to random exploration, as highlighted in orange.

4 Discussion and Conclusion

To deal with sample inefficiency and the interpretability of reinforcement learning-based robot locomotion learning, this study verifies that incorporating the neural architecture and learning algorithm with interpretability can also enhance sample efficiency and overall performance.

Considering the SME neural control, its interpretable network structure, neural activities, and synaptic connections are utilized. In terms of network structure, the SME is equipped with two interpretation dimensions. Three layers are employed to separate the network function vertically (Fig. 1a), providing layer-wise interpretation along with minimal learning parameters (i.e., only the last mapping layer), and four neuron columns are employed to separate neural activities horizontally (Fig. 1a), providing less interference of the non-neighbor robot states/movement bases [27]. The network structure with last-layer learning differs from conventional fully connected end-to-end control networks (FCNN) [5, 8, 10] and offers the following advantage. It requires fewer parameters to train, leading to faster convergence compared to full end-to-end learning (Table 2). In terms of neural activities, the generated bases exhibit less interference between distal neurons (non-neighbor neurons). This leads to 33% less interference compared to the CPGRBF neural control [14] and 10% less compared to a fully connected neural network (FCNN) with ReLU activation function (Section 2.1). Note that the FCNN, considered as a black-box control method [27], typically produces high interference activation patterns (Section S4 of the supplementary material); thus, around 17% of each neuron activity is interfered by at least one of the others. Therefore, the SME, which employs reduced interference bases further facilitates the interpretation and collective learning [20]. Finally, in terms of synaptic connections, the connection weight parameters are equipped with their own interpretations/meanings. For example, the mapping weights encode locomotion pattern/shape (as shown in Section S2 of the supplementary material) and leg coordination (as shown in Section S1 of the supplementary material), providing learning transparency and less interference update [27]. In another example,

w_τ solely represents the frequency/state transition speed parameter, further reducing the training parameters while allowing us to adjust the locomotion frequency after training (as demonstrated in https://youtu.be/Svz5H2_MDew at 2:40 mins). In terms of learning performance, the SME improves the accuracy of estimated gradients and smoothens the estimated reward landscape, leading to 65 % more reward and requiring 35 % fewer samples in comparison to SME-AGOL and CPGRBF-AGOL (Section 2.1).

Considering the learning algorithm, the proposed AGOL rule consistently exploits parameter spaces and provides explanations [32, 41] to the robot for scaling the update, allowing it to focus on more relevant parameters. Although [42] discusses various forms of gradient/relevance to adapt the learning, this study further analyzes and presents the reason for applying the absolute of gradient/relevance to adapt the parameter space exploration-based learning algorithm. The findings indicate that it can adapt the learning rule when the explored action \tilde{a}_t does not depend on the given explored parameters $\tilde{\theta}_t$ ($\nabla_{\tilde{\theta}_t} p(\tilde{a}_t | \tilde{\theta}_t) = 0$), as discussed in Section 2.2, which could further exploit the separated activities of SME. Thus, AGOL is capable of accurately estimating the weight update (control parameter update) using a small sample size (eight episodes), resulting in a smoother reward landscape with a further optimal step (Fig. 8), 38 % more reward, and 12 % fewer samples required in comparison to SME-AGOL and SME-PGPE⁺.

Table 2: Comparison of the robot training platforms and the learning time in timesteps, episodes, and simulation/real time across different locomotion learning approaches evaluated on flat terrain. #timesteps denotes the number of controller/system update steps, #episodes denotes the number of trajectories collected, and time denotes the training time without parallel training or simulation acceleration, computed from #timesteps taken until the learning converges or is reported by the original articles and the controller update rate.

Method	Trained Robot	#Motors	#Outputs	Training Time		
				#Timesteps	#Episodes	Time
[7]	sim quadruped	12	12	400m	45k	2 days
[8]	sim quadruped	12	12	30m	600k	7 days
[17]	sim quadruped	12	12	200m	1k	46 days
[11]	sim quadruped	12	12	n/a	1.2k ^a	2 days ^a
[5]	sim quadruped	12	12	1m	200	10 hrs
[10]	sim other types ^b	6	6	1.2m	1.2k	10 days
[12]	sim hexapod	18	18	n/a	2.3k	n/a
[18]	sim quadruped	12	12	2m	n/a	10 hrs
[6]	sim quadruped	12	12	400m	n/a	3 hrs
[19]	sim quadruped	12	12	35m	n/a	4 days
[15]	sim hexapod	18	18	5m	5k	2 days
[16]	sim other types ^b	3–8	3–8	1m	1k	n/a
[13]	sim quadruped	12	12	200k	100	6 hrs
[9]	sim other types ^b	3–8	3–8	100k	1k	1 hrs
[14]	sim hexapod	18	18	300k	1.2k	1.5 hrs
[14]	sim hexapod	18	9 ^c	200k	1.2k	1.5 hrs
[14]	sim hexapod	18	3 ^c	60k	200	20 mins
[22]	sim hexapod	12	6 ^c	66 ^d	n/a	5 mins ^d
SME-AGOL	real hexapod	18	18	14k	200	10 mins
	sim hexapod	18	18	10k	100	5 mins
	sim quadruped	12	12	14k	200	10 mins

^a indicates the use of guided motion.

^b indicates the use of other types of robots, e.g., hopper, half-cheetah, or bipedal robot.

^c highlights the use of output encoding where the number of network outputs is less than that of the actuators/motors.

^d indicates the use of a predefined leg pattern to learn merely interlimb coordination.

Combining SME and AGOL, locomotion learning can be achieved within 200 episodes (≈ 10 mins) directly on a physical hexapod robot starting from scratch, i.e., all parameters were initialized to zero before learning. This demonstrates sample efficient locomotion learning in the real world, which could provide an alternative method to sim2real transfer, eliminating the need for accelerated accurate simulations [7, 8] or bridging the reality gap [6]. The robot takes merely around 100 episodes (≈ 5 mins) on average to obtain a forward speed of 5 cm/s, reaching the performance benchmark obtained from a manually designed controller tested on the same robot [30]. Even on a low-friction terrain like an ice rink, the robot succeeds in learning forward locomotion under a similar timescale (not shown here but supplemented at https://youtu.be/Svz5H2_MDew). While previous works included an action smoothness reward [5, 8, 9, 14], slippage penalty [14], or clearance/collision penalty [5, 8] for smoothing the reward

landscape, SME-AGOL achieves locomotion learning on flat terrain and ice without any of these (or without a complex reward function). It uses only a simple speed-related reward to successfully learn robot locomotion within a few minutes.

The comparison in Table 2 presents that while others require either 150,000 – 400 million timesteps or up to 600,000 episodes of trial-and-error samples collected in simulation (≈ 1 hr – 46 days) [7, 8, 17], SME-AGOL demonstrates the use of merely 10,000 timesteps and 100 episodes in simulation (≈ 5 mins). Even with hexapod robots, the best performing CPGRBF neural control architecture plus the PIBB learning algorithm [14] also took 1,200 episodes (≈ 1.5 hrs) in simulation to learn independent leg patterns and 200 episodes (≈ 20 mins) to learn shared diagonal leg patterns. Due to such a long training time, SME-AGOL is among only two methods demonstrating locomotion learning on physical hexapod robots, alongside [22], which incorporates output encoding by learning/adapting merely predefined leg coordination (interlimb coordination). Therefore, SME-AGOL is the only method, to the best of our knowledge, that demonstrates sample efficient locomotion learning on a physical robot without prior knowledge. It also allows the robot to learn the patterns of all legs independently and develop both intralimb and interlimb coordination simultaneously, utilizing arbitrary trajectories within the workspace to solve the locomotion task.

The proposed SME-AGOL framework demonstrates a certain degree of generalization, allowing its direct application to different legged robot learning. The SME-AGOL method is not limited only to the tested hexapod robot since the output dimension (i.e., output mapping matrix, \mathbf{W}_b^o) can be modified for other types of robots, as shown in https://youtu.be/Svz5H2_MDew at around 3 mins (four-legged version of MORF where two middle legs were amputated) and <https://youtu.be/NwAL7jLdTc4> (Unitree B1 quadruped robot). However, its transferability across different robot platforms (learning from one type and applying to another) remains limited. While transferring the learned control policy of SME-AGOL between hexapod robots is possible, performance degradation is expected depending on the structural differences between the two robots (e.g., leg length, joint torque, and robot dynamics). Therefore, in future work, we will investigate improving SME-AGOL’s transferability through techniques like fine tuning [11] or domain randomization [6].

Apart from these aspects, multiple SMEs with in-between connections could allow the robot to learn and switch between behaviors (i.e., sets of key poses). With this mechanism, the activities in the first set can propagate to another when certain internal state neurons in the first set are inhibited by the sensory feedback, allowing the activity to propagate to another path or the second set [31]. We will investigate this in the future. More importantly, besides contributing SME-AGOL as a method for online locomotion learning, this work demonstrates the connection between interpretation and improved performance, encouraging the use of interpretation as a mechanism for obtaining understandable results and gaining a better performance toward explainable AI (XAI)-based locomotion control.

References

- [1] Ian Goodfellow, Yoshua Bengio, and Aaron Courville. *Deep learning*. MIT press, 2016.
- [2] Arthicha Srisuchinnawong, Chaicharn Akkawutvanich, and Poramate Manoonpong. Adaptive modular neural control for online gait synchronization and adaptation of an assistive lower-limb exoskeleton. *IEEE Transactions on Neural Networks and Learning Systems*, Early Access, 2023.
- [3] Arthicha Srisuchinnawong, Kitti Phongaksorn, Wasuthorn Ausrivong, and Poramate Manoonpong. Adaptive bipedal robot walking on industrial pipes under neural multimodal locomotion control: Toward robotic out-pipe inspection. *IEEE/ASME Transactions on Mechatronics*, Early Access, 2023.
- [4] Marco Tulio Ribeiro, Sameer Singh, and Carlos Guestrin. " why should i trust you?" explaining the predictions of any classifier. In *Proceedings of the 22nd ACM SIGKDD international conference on knowledge discovery and data mining*, pages 1135–1144, 2016.
- [5] Chuanyu Yang, Kai Yuan, Qiuguo Zhu, Wanming Yu, and Zhibin Li. Multi-expert learning of adaptive legged locomotion. *Science Robotics*, 5(49):2174, 2020.
- [6] Gabriel B Margolis, Ge Yang, Kartik Paigwar, Tao Chen, and Pulkit Agrawal. Rapid locomotion via reinforcement learning. *The International Journal of Robotics Research*, 43(4):572–587, 2024.
- [7] Suyoung Choi, Gwanghyeon Ji, Jeongsoo Park, Hyeongjun Kim, Juhyeok Mun, Jeong Hyun Lee, and Jemin Hwangbo. Learning quadrupedal locomotion on deformable terrain. *Science Robotics*, 8(74):eade2256, 2023.
- [8] Nikita Rudin, David Hoeller, Philipp Reist, and Marco Hutter. Learning to walk in minutes using massively parallel deep reinforcement learning. In Aleksandra Faust, David Hsu, and Gerhard Neumann, editors, *Proceedings of the 5th Conference on Robot Learning*, volume 164 of *Proceedings of Machine Learning Research*, pages 91–100. PMLR, 08–11 Nov 2022.

- [9] Annie Xie, James Harrison, and Chelsea Finn. Deep reinforcement learning amidst lifelong non-stationarity. In *4th Lifelong Machine Learning Workshop at ICML 2020*, 2020.
- [10] Fan Ding and Fei Zhu. Hliferl: A hierarchical lifelong reinforcement learning framework. *Journal of King Saud University-Computer and Information Sciences*, 34(7):4312–4321, 2022.
- [11] Laura Smith, J Chase Kew, Xue Bin Peng, Sehoon Ha, Jie Tan, and Sergey Levine. Legged robots that keep on learning: Fine-tuning locomotion policies in the real world. In *2022 International Conference on Robotics and Automation (ICRA)*, pages 1593–1599. IEEE, 2022.
- [12] Malte Schilling, Kai Konen, and Timo Korthals. Modular deep reinforcement learning for emergent locomotion on a six-legged robot. In *2020 8th IEEE RAS/EMBS International Conference for Biomedical Robotics and Biomechatronics (BioRob)*, pages 946–953. IEEE, 2020.
- [13] Aditya M Deshpande, Eric Hurd, Ali A Minai, and Manish Kumar. Deepcpg policies for robot locomotion. *IEEE Transactions on Cognitive and Developmental Systems*, 15:2105–2121, 2023.
- [14] Mathias Thor, Tomas Kulvicius, and Poramate Manoonpong. Generic neural locomotion control framework for legged robots. *IEEE transactions on Neural Networks and Learning Systems*, 32(9):4013–4025, 2020.
- [15] Yinghui Li, Jinze Wu, Xin Liu, Weizhong Guo, and Yufei Xue. Experience-learning inspired two-step reward method for efficient legged locomotion learning towards natural and robust gaits. *arXiv preprint arXiv:2401.12389*, 2024.
- [16] Ding Chen, Pfeixi Peng, Tiejun Huang, and Yonghong Tian. Fully spiking actor network with intralayer connections for reinforcement learning. *IEEE Transactions on Neural Networks and Learning Systems*, Early Access, 2024.
- [17] I Made Aswin Nahrendra, Byeongho Yu, and Hyun Myung. Dreamwaq: Learning robust quadrupedal locomotion with implicit terrain imagination via deep reinforcement learning. In *2023 IEEE International Conference on Robotics and Automation (ICRA)*, pages 5078–5084. IEEE, 2023.
- [18] Sicen Li, Yiming Pang, Panju Bai, Jiawei Li, Zhaojin Liu, Shihao Hu, Liquan Wang, and Gang Wang. Learning locomotion for quadruped robots via distributional ensemble actor-critic. *IEEE Robotics and Automation Letters*, 9, 2024.
- [19] Milad Shafiee, Guillaume Bellegarda, and Auke Ijspeert. Viability leads to the emergence of gait transitions in learning agile quadrupedal locomotion on challenging terrains. *Nature Communications*, 15(1):3073, 2024.
- [20] Richard S Sutton and Andrew G Barto. *Reinforcement learning: An introduction*. MIT press, 2018.
- [21] David Hoeller, Nikita Rudin, Dhionis Sako, and Marco Hutter. Anymal parkour: Learning agile navigation for quadrupedal robots. *Science Robotics*, 9(88):eadi7566, 2024.
- [22] Ashwin Sanjay Lele, Yan Fang, Justin Ting, and Arijit Raychowdhury. Learning to walk: Spike based reinforcement learning for hexapod robot central pattern generation. In *2020 2nd IEEE International Conference on Artificial Intelligence Circuits and Systems (AICAS)*, pages 208–212. IEEE, 2020.
- [23] Ronald J Williams. Simple statistical gradient-following algorithms for connectionist reinforcement learning. *Reinforcement learning*, pages 5–32, 1992.
- [24] Frank Sehnke, Christian Osendorfer, Thomas Rückstieß, Alex Graves, Jan Peters, and Jürgen Schmidhuber. Parameter-exploring policy gradients. *Neural Networks*, 23(4):551–559, 2010.
- [25] John Schulman, Filip Wolski, Prafulla Dhariwal, Alec Radford, and Oleg Klimov. Proximal policy optimization algorithms. *arXiv preprint arXiv:1707.06347*, 2017.
- [26] Freek Stulp and Olivier Sigaud. Policy improvement methods: Between black-box optimization and episodic reinforcement learning. *hal-00738463*, 2012.
- [27] Claire Glanois, Paul Weng, Matthieu Zimmer, Dong Li, Tianpei Yang, Jianye Hao, and Wulong Liu. A survey on interpretable reinforcement learning. *Machine Learning*, pages 1–44, 2024.
- [28] Arthicha Srisuchinnawong, Jettanan Homchanthanakul, and Poramate Manoonpong. Neurovis: real-time neural information measurement and visualization of embodied neural systems. *Frontiers in Neural Circuits*, 15:743101, 2021.
- [29] Mathias Thor and Poramate Manoonpong. Versatile modular neural locomotion control with fast learning. *Nature Machine Intelligence*, 4(2):169–179, 2022.
- [30] Jettanan Homchanthanakul and Poramate Manoonpong. Continuous online adaptation of bioinspired adaptive neuroendocrine control for autonomous walking robots. *IEEE Transactions on Neural Networks and Learning Systems*, 33(5):1833–1845, 2021.

- [31] Mathias Lechner, Ramin Hasani, Manuel Zimmer, Thomas A Henzinger, and Radu Grosu. Designing worm-inspired neural networks for interpretable robotic control. In *2019 International Conference on Robotics and Automation (ICRA)*, pages 87–94. IEEE, 2019.
- [32] Grégoire Montavon, Alexander Binder, Sebastian Lapuschkin, Wojciech Samek, and Klaus-Robert Müller. Layer-wise relevance propagation: an overview. *Explainable AI: interpreting, explaining and visualizing deep learning*, pages 193–209, 2019.
- [33] Jost Tobias Springenberg, Alexey Dosovitskiy, Thomas Brox, and Martin Riedmiller. Striving for simplicity: The all convolutional net. In *ICLR (workshop track)*, 2015.
- [34] Mathias Thor, Jørgen Christian Larsen, and Poramate Manoonpong. Morf—modular robot framework. In *Proc. 2nd Int. Youth Conf. Bionic Eng.(IYCBE)*, pages 21–23, 2018.
- [35] Eric Rohmer, Surya PN Singh, and Marc Freese. V-rep: A versatile and scalable robot simulation framework. In *2013 IEEE/RSJ international conference on intelligent robots and systems*, pages 1321–1326. IEEE, 2013.
- [36] Emanuel Todorov, Tom Erez, and Yuval Tassa. Mujoco: A physics engine for model-based control. In *2012 IEEE/RSJ international conference on intelligent robots and systems*, pages 5026–5033. IEEE, 2012.
- [37] Maximilian Hensel. *Correlated Exploration in Deep Reinforcement Learning*. PhD thesis, Technische Universität Darmstadt, 2019.
- [38] Matthias Plappert, Rein Houthoofd, Prafulla Dhariwal, Szymon Sidor, Richard Y Chen, Xi Chen, Tamim Asfour, Pieter Abbeel, and Marcin Andrychowicz. Parameter space noise for exploration. *arXiv preprint arXiv:1706.01905*, 2017.
- [39] Adam Paszke, Sam Gross, Soumith Chintala, Gregory Chanan, Edward Yang, Zachary DeVito, Zeming Lin, Alban Desmaison, Luca Antiga, and Adam Lerer. Automatic differentiation in pytorch. In *Conference on Neural Information Processing Systems*, 2017.
- [40] Andrew Ilyas, Logan Engstrom, Shibani Santurkar, Dimitris Tsipras, Firdaus Janoos, Larry Rudolph, and Aleksander Madry. A closer look at deep policy gradients. In *International Conference on Learning Representations*, 2020.
- [41] Ramprasaath R Selvaraju, Michael Cogswell, Abhishek Das, Ramakrishna Vedantam, Devi Parikh, and Dhruv Batra. Grad-cam: Visual explanations from deep networks via gradient-based localization. In *Proceedings of the IEEE international conference on computer vision*, pages 618–626, 2017.
- [42] Jin Ha Lee, Ik hee Shin, Sang gu Jeong, Seung-Ik Lee, Muhamamad Zaigham Zaheer, and Beom-Su Seo. Improvement in deep networks for optimization using explainable artificial intelligence. In *2019 International Conference on Information and Communication Technology Convergence (ICTC)*, pages 525–530. IEEE, 2019.

Supplementary Material

S1 Example of Leg Coordination Patterns

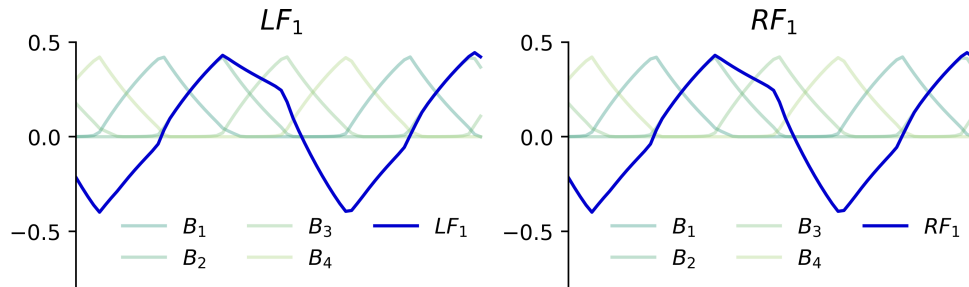


Figure S1: (left, blue) LF_1 and (right, blue) RF_1 commands, presented along with their shared bases (green), when the mapping weights from the bases to LF_1 are set to $\{0, 1, 0.5, -1\}$ and those to RF_1 are set to $\{0, 1, 0.5, -1\}$. This demonstrates the generation of same-phase patterns. Note that the mapping weights are presented as $\{w_1, w_2, w_3, w_4\}$, where w_i denotes a mapping weight from the i^{th} basis to the output (LF_1 or RF_1), and the i^{th} key pose is $\approx 0.5 \cdot w_i$.

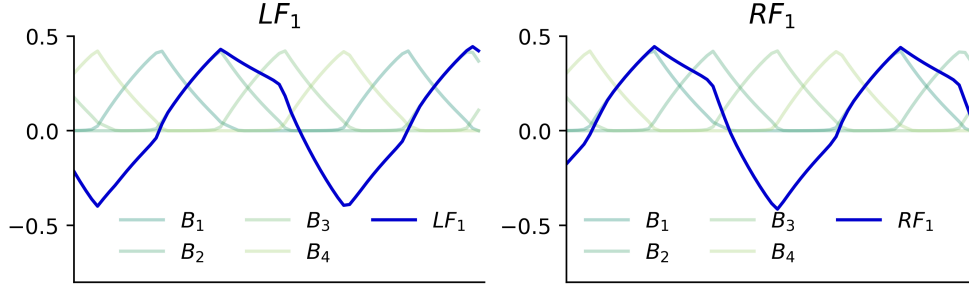


Figure S2: (left, blue) LF_1 and (right, blue) RF_1 commands, presented along with their shared bases (green), when the mapping weights from the bases to LF_1 are set to $\{0,1,0.5,-1\}$ and those to RF_1 are set to $\{1,0.5,-1,0\}$. This demonstrates the generation of 90° -phase different patterns. Note that the mapping weights are presented as $\{w_1, w_2, w_3, w_4\}$, where w_i denotes a mapping weight from the i^{th} basis to the output (LF_1 or RF_1), and the i^{th} key pose is $\approx 0.5 \cdot w_i$.

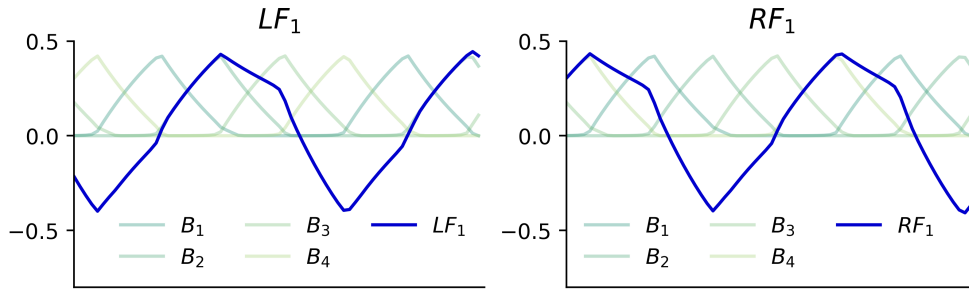


Figure S3: (left, blue) LF_1 and (right, blue) RF_1 commands, presented along with their shared bases (green), when the mapping weights from the bases to LF_1 are set to $\{0,1,0.5,-1\}$ but those to RF_1 are set to $\{-1,0,1,0.5\}$. This demonstrates the generation of anti-phase patterns. Note that the mapping weights are presented as $\{w_1, w_2, w_3, w_4\}$, where w_i denotes a mapping weight from the i^{th} basis to the output (LF_1 or RF_1), and the i^{th} key pose is $\approx 0.5 \cdot w_i$.

S2 Example of Different Leg Pattern

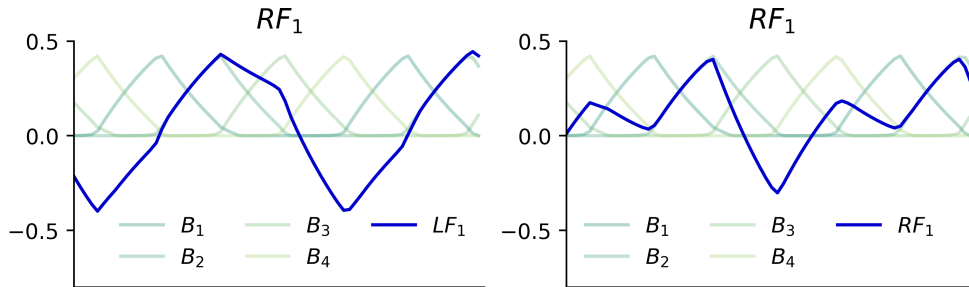


Figure S4: (blue) RF_1 command, presented along with (green) the shared bases, when the mapping weights from the bases to RF_1 are set to (left) $\{0,1,0.5,-1\}$ and (right) $\{0,1,-0.8,0.5\}$. This demonstrates the generation of different shape patterns. Note that the mapping weights are presented as $\{w_1, w_2, w_3, w_4\}$, where w_i denotes a mapping weight from the i^{th} basis to the output: RF_1 , and the i^{th} key poses is $\approx 0.5 \cdot w_i$.

S3 CPGRBF neural control

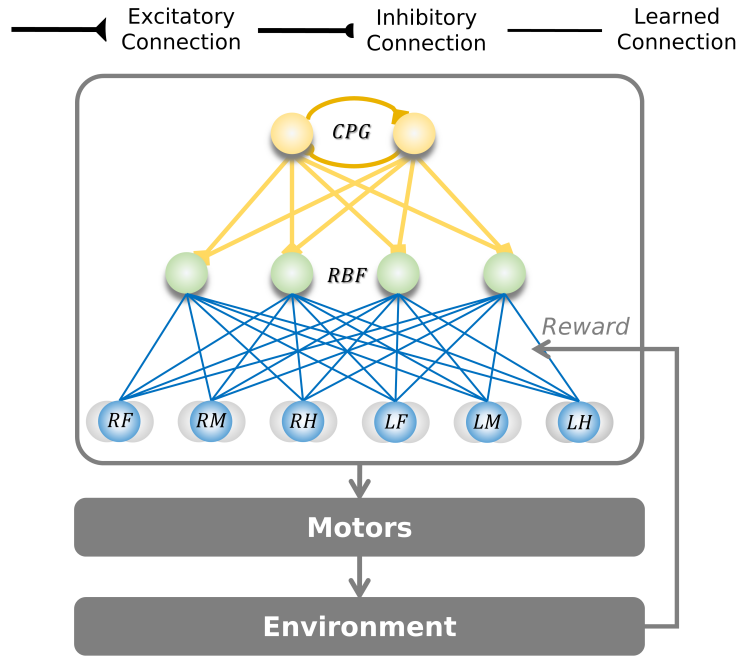


Figure S5: The structure of the CPGRBF neural control employed in the experiment, where CPG is a two-neuron oscillator network acting as the central pattern generator and RBF is a radial basis function network acting as the output mapping.

S4 The Activities of Fully Connected Neural Network

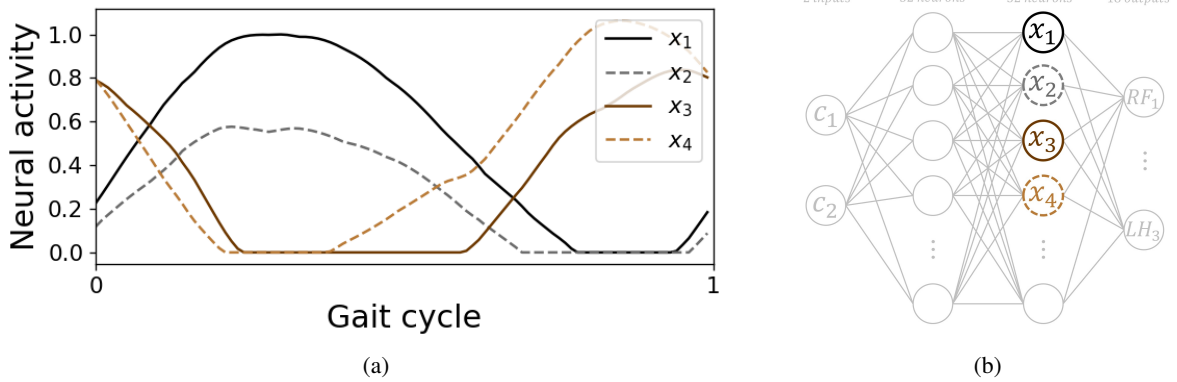


Figure S6: (a) An example of the four neural activities (i.e., x_1-x_4) of the last hidden layer of (b) a fully-connected neural network (FCNN) with 1.7k parameters and the ReLU activation function trained for 100 episodes. We can see several overlapping of neural activities within a gait cycles. This shows that 17% of each neuron activity is interfered by at least one of the others, which leads to inefficient learning in FCNN [5, 8, 10].